JOURNAL OF MATERIALS SCIENCE 32 (1997) 4085–4099

Topological properties of polymer spherulitic grain patterns from simultaneous nucleation

M. R. KAMAL*, TAO HUANG, A. D. REY
Department of Chemical Engineering, McGill University, 3480 University Street, Montreal, Quebec, Canada H3A 2A7

Experimental and theoretical characterization of large-scale spherulitic grain patterns of isotactic polypropylene have been carried out under simultaneous nucleation conditions. Rigorous image analysis has been performed to characterize the topological correlation of grain-boundary shapes and grain sizes, as well as topological rearrangements during thermal activation experiments. The topological and geometrical aspects of the spherulitic grains are subjected to a comprehensive analysis, using the characterization methodology commonly employed in studies of random cellular patterns. A distinguishing feature of polymer grain patterns is the presence of topological defects. Topological defects have been identified by using standard computational geometry method such as the multigraphic construction of the grain-boundary network (GBN) and its relevant dual, the nearest-neighbour network. The topological defects are the mixed configurations of vertices containing three, four, five and six connectives, where the fraction of trivalent vertices is smaller than 1. It is found firstly that the two-cell correlation functions $M_k(n)$ (the average number of k-sided grains adjoining an n-sided grain), are clearly highly non-linear with n, secondly that the common practice of plotting $nm(n)$ versus n can conceal the non-linearity of the experimental data, where $m(n)$ is the average sum of the number of sides of the grains immediately adjacent to an n-sided grain and thirdly that the plot of the relation of average area of grains to the number of sides is non-linear and S-shaped, owing to the polydisperse grain packing. These topological and geometrical characteristics indicate that the polymer GBN does not follow either the mathematical Voronoi diagram or the common random cellular structures displayed in many physical systems. Thermal activation experiments show that the polymer grain pattern is a topological unstable structure with very slow dynamics. Finally, these experimental observations are explained in relation to specific polymeric features.

1. Introduction

It is well known that, when semicrystalline polymer samples are crystallized from the bulk, the most frequently observed structure is the spherulitic polygrain pattern. The spherulites are composed of individual nanometre-scale lamellar crystalline plates interspersed with amorphous regions. The properties of the semicrystalline polymer depend on the microstructure, which is defined not only by the lamellar structure on the nanometre scale but also by the spherulitic grain pattern on the micrometre scale.

The microstructure of spherulitic grains solidified from the melt as a polymer film exhibits a random cellular pattern with a random distribution of areas and number of sides [1, 2]. Such two-dimensional (2D) space-filling random cellular patterns are encountered in many scientific fields [3, 4]. Recent thorough experimental and theoretical studies have been devoted to the evolution of cellular patterns, such as soap froths [5, 6] and the coarsening of polycrystals [7–9], and to the characterization and understanding of the topological properties of 2D cellular structures [10–17]. Normally, the cellular patterns are characterized by topological elements and geometrical elements. The basic topological elements of the cellular patterns are the edges (or sides), faces and vertices of the cells, while the basic geometrical elements are the areas and perimeters of the cells. The basic statistical measures of cellular structures are the topological side distribution and the geometrical area distribution. In spite of their fundamental importance, the formation and evolution of polymer grain patterns have not received great attention so far.

In an earlier study [1, 2], we reported the experimental characterization of the topological organization of the highly disordered polygrains in planar films formed during free solidification of a common model polymer, isotactic polypropylene. The distinct features

*Author to whom all correspondence should be addressed.

0022–2461

of the polymer spherulitic polygrains were evaluated in order to test the validity and deviations of two commonly used scaling laws: the Aboav–Weaire relation [3] and the Lewis–Rivier relation [3]. It was found that the cellular grain patterns of isotactic polypropylene exhibit strong deviations from the two laws. Also, it was found that the five-sided grains, and not six-sided grains, dominate the microstructure of the polypropylene spherulitic polygrain system. In addition, evidence was presented for firstly the existence of lenses (two-sided grains, $n = 2$), which are rarely present in other cellular structure systems, and secondly the absence of many-sided ($n > 10$) polygrains, which are usually present in most systems. Analysis by spatial tessellation showed that the temporal evolution and spatial distribution of nuclei point patterns play a role in the formation of the grain-boundary networks (GBNs) in the polypropylene spherulitic polygrains.

Polymer spherulitic grain development gives rise to a variety of complex structures. In order to obtain a basic understanding of the representative topological characteristics of polymer spherulitic grain patterns as random cellular structures, we have continued to study the free solidification of isotactic polypropylene during isothermal crystallization and simultaneous nucleation. This system gives rise to the simplest polymer grain networks owing to the constant growth velocity and simultaneous nucleation of all spherulities. Scrupulous image analysis was performed to characterize the topological correlations and geometrical distributions of grain-boundary shapes and grain sizes, as well as the topological rearrangement during thermal activation experiments.

2. Experimental techniques

Direct experimental investigation of polygrains requires real-time *in-situ* observations. Unlike metals and ceramics, accurate measurements and observations could be performed by using transparent crystal systems [8]. The slow dynamics and transparency of polymeric systems permit accurate measurements and observations during all stages of grain pattern formation and evolution. Digital image processing has greatly improved our ability to analyse large numbers of grains. Counting and size measurements are simplified substantially.

2.1. Material

Experiments were carried out with a common model polymer, isotactic polypropylene (iPP), which was purchased from Aldrich Chemical Company Inc. (Catalogue No. 18238-9). The iPP employed in the present study had the following properties: molecular weight, $M_\eta = 2.7 \times 10^5$; degree of crystallinity, 38 wt%; glass transition temperature, $T_g = 269.6$ K; melting temperature, $T_m = 439$ K. A polymer thin film 20 μm thick was formed by pressing the melt between two glass slides.

2.2. Optical measurements and image analysis

A polarizing microscope (Leitz Laborlux 12), equipped with a Leitz hot stage for polymer film solidification, was used for direct observation during experiments. The temperatures of isothermal solidification are controlled to within $\pm 0.1\,^{\circ}$C, in order to obtain the simultaneous nucleation and constant growth velocity. System stability on a practical time scale was established by periodically monitoring the sample over a 6 month period. Unlike polycrystalline metals or ceramics, the network of iPP polygrains did not exhibit detectable change during 6 months at room temperature. When the sample was held at 50 °C for 6 weeks, changes were still not detectable. These results indicate that the uniform grain-boundary mobility is zero at these temperatures. In order to observe the topological stability of the grain organization and the topological rearrangement, thermal activation experiments were carried out by heating the sample to 150 °C and then holding isothermally at this temperature for several hours to observe the changes in the vertex configurations and grain boundaries.

A JAVA–Jandel Scientific video measurement and image processing system was directly connected to the microscope via a charge-coupled device camera. This image-processing system made it possible to capture the images of pattern growth and polygrain formation during solidification processing and allowed for enhancement of the edges if necessary. The system also executed statistical data processing from the various experiments and provided output of both data and images.

In order to perform automatic grain counting and size measurements, the digitized image should be converted into a binary image of grain boundaries by defining the grain perimeter and deleting the spherulite inside texture by contrast enhancement for every grain. The image quality obtained was sufficiently good, so that there were no spurious grains or broken lines. The next stage was to perform automatic grain counting and size measurements. 30 images were selected from each experimental run. The statistical data were obtained from around 5000 grains, and the error in measuring grain areas was less than 5%. Each grain was labelled for further analysis. The description of the shapes and the sizes of polygrain patterns involved side and area distributions, and topological relationships.

3. Theoretical background

There are two basic types of random cellular systems:

(a) evolutive physical cellular network patterns, where the number of cells and sometimes the total area change with time, such as 2D soap froths in fluid mechanics and the coarsening of polycrystals in metallurgy;

(b) non-evolutive mathematical random cellular pattern, where the number of cells (and total space) remains constant, such as the Voronoi diagram [18] in computational geometry (tessellation built from point assemblies).

Cells in 2D infinite space-filling structures usually have at least three sides, and a rather regular geometric shape with cell vertices belonging to three cells. The topology of cellular networks imposes constraints on the possible configurations of the cells. For example, for the probability distribution, $P(n)$, of the number, n, of edges of cells and for the two-cell correlation, $M_k(n)$ (the average number of k-sided neighbours of an n-sided cell), the following constraints hold [12].

1. $\sum_n P(n) = 1$, the trivial constraint on probabilities.

2. $\langle n \rangle = \sum_n nP(n) = 6$, Euler's topological constraint for trivalent vertices.

3. $\sum_k M_k(n) = n$, as an n-sided cell always has n neighbours in total.

In this section, we review the basic theoretical background for both physical random cellular networks and a mathematical spatial tessellation diagram (the classical Voronoi diagram) as the starting point for the topological characterization of the polymer spherulitic polygrain system. Detailed description of some of the concepts involved may be found elsewhere [3–18].

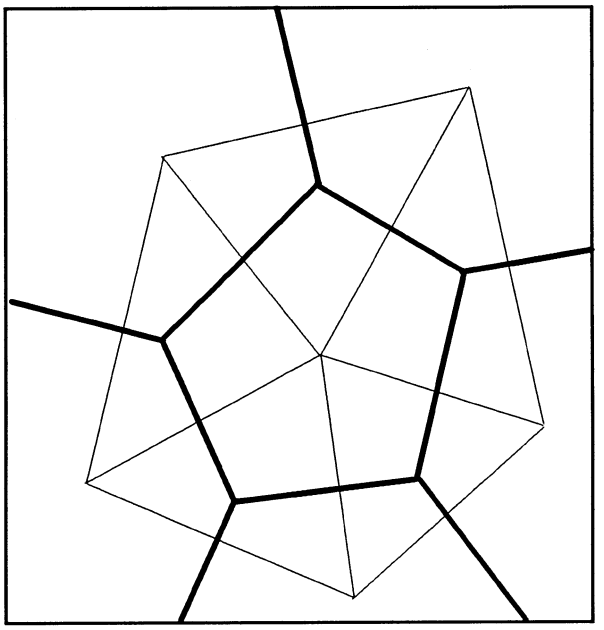

Figure 1 The dual of the Voronoi diagram (the thick-line network) is the Delaunay triangulation (the thin-line network).

3.1. Voronoi diagrams and Delaunay triangulation

Consider a set of points $P = \{p_1, p_1, \ldots, p_i\}$ in the 2D Euclidean plane, called the sites. We subdivide the plane into portions $V(p_i)$, in such a way that all points in each portion are nearer to p_i than to any p_j: $V(p_i) = \{p \,|\, \mathrm{dist}(p, p_i) < \mathrm{dist}(p, p_j) \quad \forall j \neq i\}$. This results in partitioning the plane by assigning every point in the plane to its nearest site. All the points assigned to p_i from the Voronoi region $V(p_i)$. Since the Voronoi regions $V(p_i)$ are the intersections of $n - 1$ half-planes, they are convex polygons with straight-line edges, the perpendicular bisectors of p_i and p_j. This construction is called the Voronoi diagram [18]. The Voronoi diagram is a tessellation built from point (site) assemblies, so that Voronoi polygons correspond to the sites. Each point on an edge is equidistant from exactly two sites. Normally, the vertices of Voronoi regions are trivalent because every vertex belongs to three Voronoi polygons. Each vertex is equidistant from three sites.

In a graph-theoretical sense [17], the Voronoi diagram is a plane network and a connectivity-three graph because Voronoi regions are connected by three lines whose end point is a trivalent vertex, as mentioned above. To gain insight regarding this complex graph of network cells, it is important to have a thorough understanding of the duality relation between network cells. Fig. 1 shows this duality relation schematically. In Fig. 1, the network with the thick solid lines is the real-space graph (the Voronoi diagram) and the network with thin solid lines (the Delaunay triangulation) is the dual network. The duality relationship maps all cells of the graph to a vertex in the dual network, all vertices to the faces of the dual, and the edges to edges. If vertices in the real-space graph are triply connected, the faces of the dual network are triangles, and the dual is a triangulation as shown in Fig. 1. The dual of the Voronoi diagram $V(P)$ is the Delaunay triangulation $D(P)$. Delaunay triangulation $D(P)$ produces a planar triangulation of the Voronoi sites P. It contains an edge (straight line) connecting two sites in the plane if and only if their Voronoi regions share a common edge. Consider all triangles formed by the sites such that the circumcircle of each triangle is empty of other sites. The set of edges of these triangles gives the Delaunay triangulation of the sites.

Because the $D(P)$ and $V(P)$ are dual structures, each contains the same "information" in some sense, but represented in rather different form. Mathematically, the triangulation has been investigated extensively in graph theory and lattice theory, as well as in computational geometry. The triangulation is a better way of describing the real-space graph for some purposes, because it is much simpler than the polygon network. Additionally, the vertices of the triangulation are associated with the faces of the real-space network, which are the areas of the cells. The description of the vertices of the triangulation is more convenient.

It must be mentioned that the duality relationship between both topological descriptions does not hold for all networks. Firstly, there are actually other networks with connectivity three, but where the given number of the cells is more than triangulations with a given number of vertices. This occurs, for example, if there are lenses in the real-space network. Secondly, the Delaunay triangulation $D(P)$ is a triangulation only if no more than three sites are cocircular, for example, if there are multiple vertices in the real-space networks. Graphs are not allowed to have these two cases. Networks which are not graphs are called multigraph [17]. We shall use this property in Section 4 to identify the topological defects in polymer spherulitic grain patterns.

3.2. The Aboav–Weaire law

Many physical random cellular networks have similar structures and evolve to a steady state, characterized by a scaling (stationary) distribution of cell sizes, shapes and correlation. The similarity of the scaling state across systems moulded by different physical forces has led many workers to seek an explanation independent of the driving forces [3, 4]. Among the properties of the scaling state, the probability, $P(n)$, of cells with n sides is the most frequently measured in experimental systems. The best-obeyed empirical regularity pertains to two-cell correlations. The Aboav–Weaire law [3] states that on average the sum of the number of sides of the cells immediately adjacent to an n-sided cell, $nm(n)$, is linear in n:

$$nm(n) = (6 - a)n + (6a + \mu_2) \quad (1)$$

where μ_2 is the second moment of the $P(n)$ distribution. The second moment is defined as $\mu_2 = \sum_n P(n)(n - \langle n \rangle)^2$, where $\langle n \rangle$ is the average with respect to the same distribution, $P(n)$, and whose variance, $\mu_2 = \langle n^2 \rangle - \langle n \rangle^2$, is a convenient measure of topological disorder. The first moment for networks of trivalent vertices must be 6.

The Aboav–Weaire law consists of three assertions:

(i) $nm(n)$ is linear in n.

(ii) The slope of $nm(n)$ is approximately 5, i.e., $a \approx 1$ (empirically).

(iii) Regardless of the slope of $nm(n)$, the following relation holds: $6m(6) = 36 + \mu_2$.

The last assertion is a direct result [12] of the linearity of $nm(n)$. Although maximum-entropy theory and microreversibility arguments [10] establish a theoretical basis for the linearity mentioned above, the value of the slope observed in experimental studies remains unexplained [12–17]. On the other hand, for finite networks $\langle n \rangle \neq 6$, the topological model gives the relation [15]

$$nm(n) = (\langle n \rangle - a)n + [\langle nm(n) \rangle - \langle n \rangle^2 + \langle n \rangle a] \quad (2)$$

The Aboav–Weaire law does not apply to the Voronoi diagram. Instead, computer simulations [19] for a set of 2D Poisson distributed sites shows that a quadratic function fits well:

$$m(n) = q + \frac{b}{n} + \frac{c}{n^2} \quad (3)$$

The values of the three parameters are $q = 5.01$, $b = 9.68$ and $c = -11.18$.

3.3. The Lewis–Rivier law

Besides the topological description, the number of sides n is relevant for both geometrical and physical reasons. The size of the cells measured by perimeter and area is an important aspect of random physical cellular structures. The correlation between the sizes and the shapes of the cells is described by the relation between average area, $\langle a_n \rangle$, and the number of the sides. Lewis [20, 21] (see also [3]) found that the average area, $\langle a_n \rangle$, of n-sided cells increases monotonically with increasing n. Rivier [10] presented a theoretical treatment based on the maximum-entropy principle that also predicts a linear relationship between $\langle a_n \rangle$ and n The resulting Lewis law of Lewis–Rivier relation is an empirical linear relationship between the average area, $\langle a_n \rangle$, and n:

$$\langle a_n \rangle = 1 + \lambda(n - 6) \quad (4)$$

where λ is the gradient. For 2D Poisson–Voronoi diagram, $\lambda = \frac{1}{4}$. Statistical thermodynamics analysis gives a different exponent: $\langle a_n \rangle \propto n^2$ [22, 23]. The random-neighbour model [24] shows the linear relationship as an asymptotic law for large n ($n > 6$). Unfortunately, experimental results are not conclusive.

4. Grain-boundary multigraph and topological defects

In this section, we characterize the multigraphic construction of the GBN and its dual nearest-neighbour network (NNN) in order to identify the topological defects in iPP spherulitic grain patterns.

4.1. Spherulitic grain formation

Fig. 2 presents a series of images that show the typical process of pattern formation of the network of grain boundaries during isothermal crystallization of isotactic polypropylene at 135 $\pm$ 0.1 °C. The images indicate the following three steps in the crystallization process:

(i) the simultaneous nucleation;

(ii) multispherulitic growth;

(iii) impingement.

Simultaneous nucleation means that all the nuclei are formed at the same time. Every spherulite grows with the same constant front velocity. When two or more spherulites meet, impingement consisting of "growth–touch–stop" occurs. The interspherulitic boundaries are formed during this impingement step. When the impingement step is finished, the 2D network of grain boundaries is eventually formed. Almost all the edges of grains are straight lines and are the bisectors of the nuclei (the sites).

4.2. Graphic description

In order to characterize the complex structures of spherulitic grain patterns, it is necessary to have a through understanding of the relationships between the GBN and the corresponding NNN of nuclei centre points. As an example, we show in Fig. 3a the 2D GBN obtained by edge tracking the image of Fig. 2h. This 2D GBN has the appearance of a Voronoi diagram. Analysis of spatial tessellation by image processing confirms that the edges of the GBN are the straight-line bisectors of the sites (the centres of nuclei). Fig. 3b is the combination of the GBN (the thick line) and the NNN (the thin line) constructed by the nearest-neighbour searching. The NNN resembles the dual of GBN. Fig. 3b presents a duality which looks like Fig. 1. However, Fig. 3b clearly shows that

the GBN is not a complete connectivity-three network because, in many instances, more than three sites are cocircular. For example, in Fig. 4, which is a local image taken from Fig. 2h, the cocircularity of the sites was tested by the graphic function of Microsoft Words® software. The analysis shows that it contains two four-point cocircle and one six-point cocircles in the middle right. Fig. 4 shows that the multiple cocircularity of the sites is due to the presence of the fourfold, fivefold and sixfold vertices. For example, the upper circle shows the presence of a fourfold vertex, and the middle circle shows the presence of a sixfold vertex.

From the above analysis, a special characteristic of the spatial arrangement of the polymer GBN is that there is a high density of *singular vertices*, which are mixed configurations containing vertices with $z = 3, 4, 5, 6$, where z is the connectivity. Thus the fraction of trivalent vertices, $f_{z=3}$, is less than one: $f_{z=3} < 1$. For example, the fraction of trivalent vertices for the nearest-neighbour graph shown in Fig. 3 is $f_{z=3} = 0.6731$. Fig. 5 shows the NNN corresponding to the GBN network shown in Fig. 3. The full circles represent the polygons which are not triangles and arise from the non-trivalent vertices. Fig. 6 shows the ratio of $z > 3$ vertices to $z = 3$ vertices corresponding to the number of grain sides, n. The figure shows that four-sided grains have more multiple vertices. As topological defects, multiple vertices are structurally unstable with respect to both topology and physical dynamics.

5. Topological correlation

In this section, we characterize the topological correlation of iPP spherulitic grain patterns and explore the deviations of the experimental results from the Aboav–Weaire relation. Below we discuss the probability distribution function of two-grain arrangements, and the effects of topological defects (such as multiple vertices) on topological correlation.

5.1. Definitions

Three correlation functions will be considered:

(i) the local grain correlation function, $m_l^j(n)$, which is the average number of sides of the neighbours of the jth considered n-sided grain, where l is the number of the neighbours, and where $l = n$ for the connectivity-three cellular patterns;

(ii) the two-grain correlation functions, $M_k(n)$, which is the average number of k-sided grains adjoining an n-sided grain

(iii) the Aboav–Weaire relation (see Section 3 and Equation 1), where $m(n)$ is the average sum of the number of sides of the grains immediately adjacent to an n-sided grain.

From the definition, we have

$$m(n) = \frac{1}{N_n}\sum_{j}^{N_n} m_l^j(n) \tag{5a}$$

where N_n is the total number of the considered n-sided grains.

For the connectivity-three cellular pattern, the following relationships hold [12]:

$$\sum_k M_k(n) = n \tag{5b}$$

$$nm(n) = \sum_k M_k(n)k \tag{5c}$$

As a topological defect, singular vertices (vertices with $z > z_s = 3$) in polymer spherulitic grain patterns introduce new features in the topological correlation functions. More specifically, the topological defects introduce complications in the analysis of the local grain correlation and the two-grain correlation. It turns out that there are two types of neighbour in the topological network for a corresponding grain (n grain) which has singular vertices:

(i) *unconditional neighbours*: associated n grains that share one side with the grain under consideration;

(ii) *conditional neighbours*: associated grains that share one multiple vertex ($z > 3$) with the grain under consideration.

In order to gain some insight of the influences of the singular vertices on the local grain correlation, we show in Fig. 7 a typical situation arising in actual polymer cellular patterns. The central grain in Fig. 7a is a five-sided grain. It has five nearest neighbours which are unconditional and associated n grains which share one side with the grain under consideration. Because there is a four-fold vertex (indicated by a circle) on this central grain, it has also one conditional neighbour (dotted grain). The conditional neighbour is a five-sided grain that shares one fourfold vertex with five-sided central grain. The presence of a multiple vertex suggests two ways to calculate the local grain correlation.

(a) *The unconditional local grain correlation*, $m_l^j(n, \mathrm{u})$, is calculated from the following equation:

$$m_l^j(n, \mathrm{u}) = \sum_{k=3}\frac{1}{l}(i_{kj}^{\mathrm{u}} \times k) = \sum_{k=3}\frac{1}{n}(i_{kj}^{\mathrm{u}} \times k) \tag{6a}$$

where i_{kj}^{u} is the number of the k-sided unconditional neighbours of the jth considered grain, and where l is the number of the unconditional neighbours. For example, for the central grain in Fig. 7a, $m_5(5, \mathrm{u}) = (3 \times 5 + 1 \times 6 + 1 \times 7)/5 = 5.6$.

(b) *The unconditional plus conditional local grain correlation*, $m_l^j(n, \mathrm{u} + \mathrm{c})$, is calculated from the following equation:

$$m_l^j(n, \mathrm{u} + \mathrm{c}) = \sum_{k=3}\frac{i_{kj}^{\mathrm{u}} + i_{kj}^{\mathrm{c}}}{n + l_{\mathrm{c}}} \times k \tag{6b}$$

where $i_{kj}^{\mathrm{u}} + i_{kj}^{\mathrm{c}}$ is the sum of the numbers of the k-sided unconditional plus conditional neighbours of the jth considered grain, and where l_{c} is the number of conditional neighbours. In Fig. 7a, the considered central five-sided grain has five unconditional neighbours and one conditional neighbour, $l_{\mathrm{c}} = 1$; therefore, $m_5(5, \mathrm{u} + \mathrm{c}) = ((3 + 1) \times 5 + 1 \times 6 + 1 \times 7)/(5 + 1) = 5.5$.

If we apply the vertex decay operation to the multiple vertex in Fig. 7a, which transforms the multiple vertex to three-connective vertices, as shown as Fig. 7b, the pattern becomes a pure three-connective

network, and the pure local grain correlation is $m_5(5) = (1 \times 5 + 3 \times 6 + 1 \times 7)/5 = 6$. This clearly shows that the local grain correlation of the grain pattern in the presence of singular vertices is different from the defect-free network.

5.2. Analysis

Substituting Equations 6a and 6b into Equation 5a, the average values of local grain correlations are given by

$$m(n, \mathrm{u}) = \frac{1}{N_n} \sum_{j=1}^{N_n} m_l(n, \mathrm{u}) = \frac{1}{N_n} \sum_{j=1}^{N_n} \sum_{k=3} \frac{1}{n} (i_{kj}^{\mathrm{u}} \times k) \tag{7a}$$

$$m(n, \mathrm{u} + \mathrm{c}) = \frac{1}{N_n} \sum_{j=1}^{N_n} m_l(n, \mathrm{u} + \mathrm{c}) = \frac{1}{N_n} \sum_{j=1}^{N_n} \sum_{k=3} \frac{i_{kj}^{\mathrm{u}} + i_{kj}^{\mathrm{c}}}{n + l_{\mathrm{c}}} \times k \tag{7b}$$

Likewise, from the definition of two-grain correlation, we have the following equations:

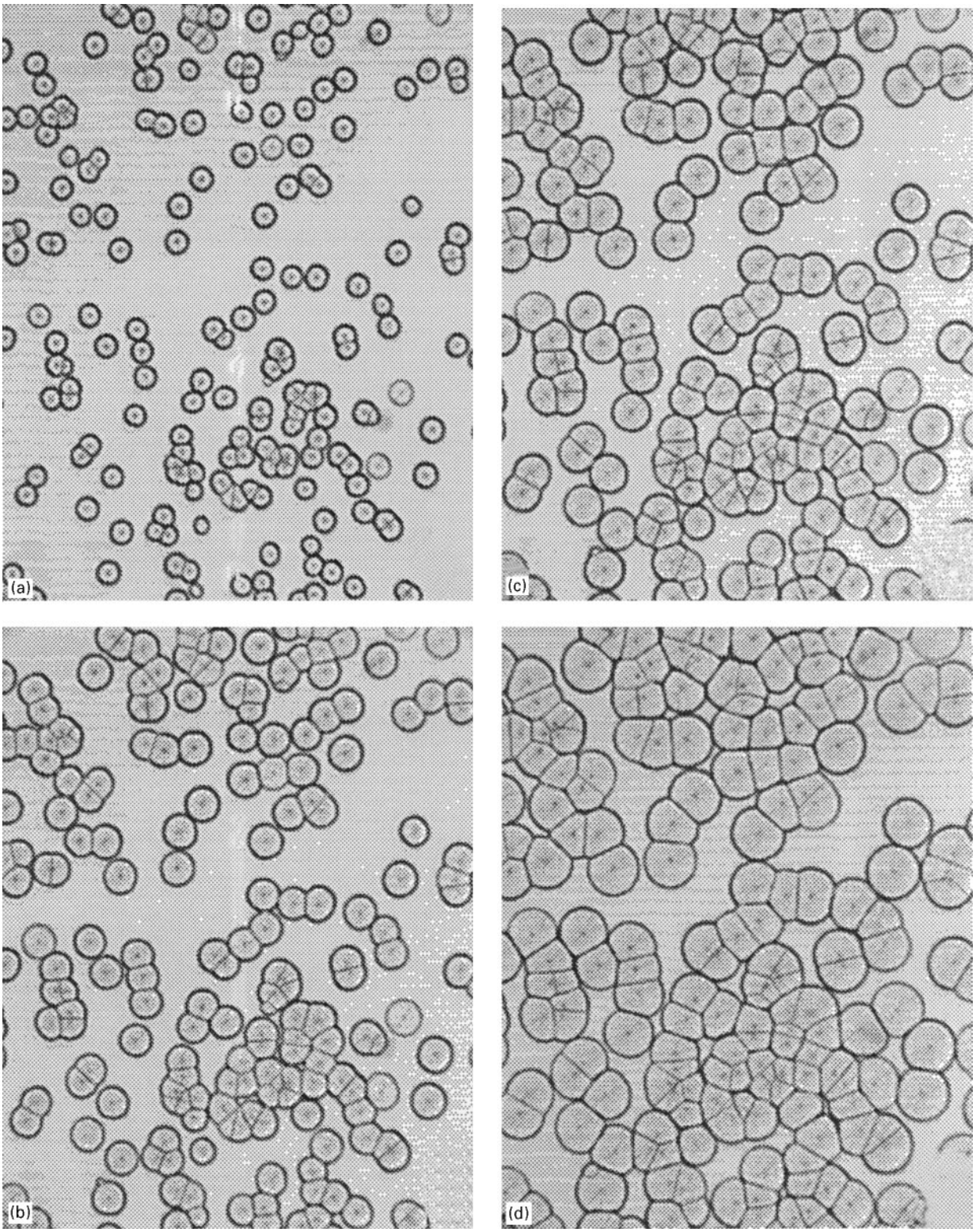

Figure 2 A series of images of the typical process of pattern formation of the network of grain boundaries during isothermal crystallization of iPP at 135 ± 0.1 °C.

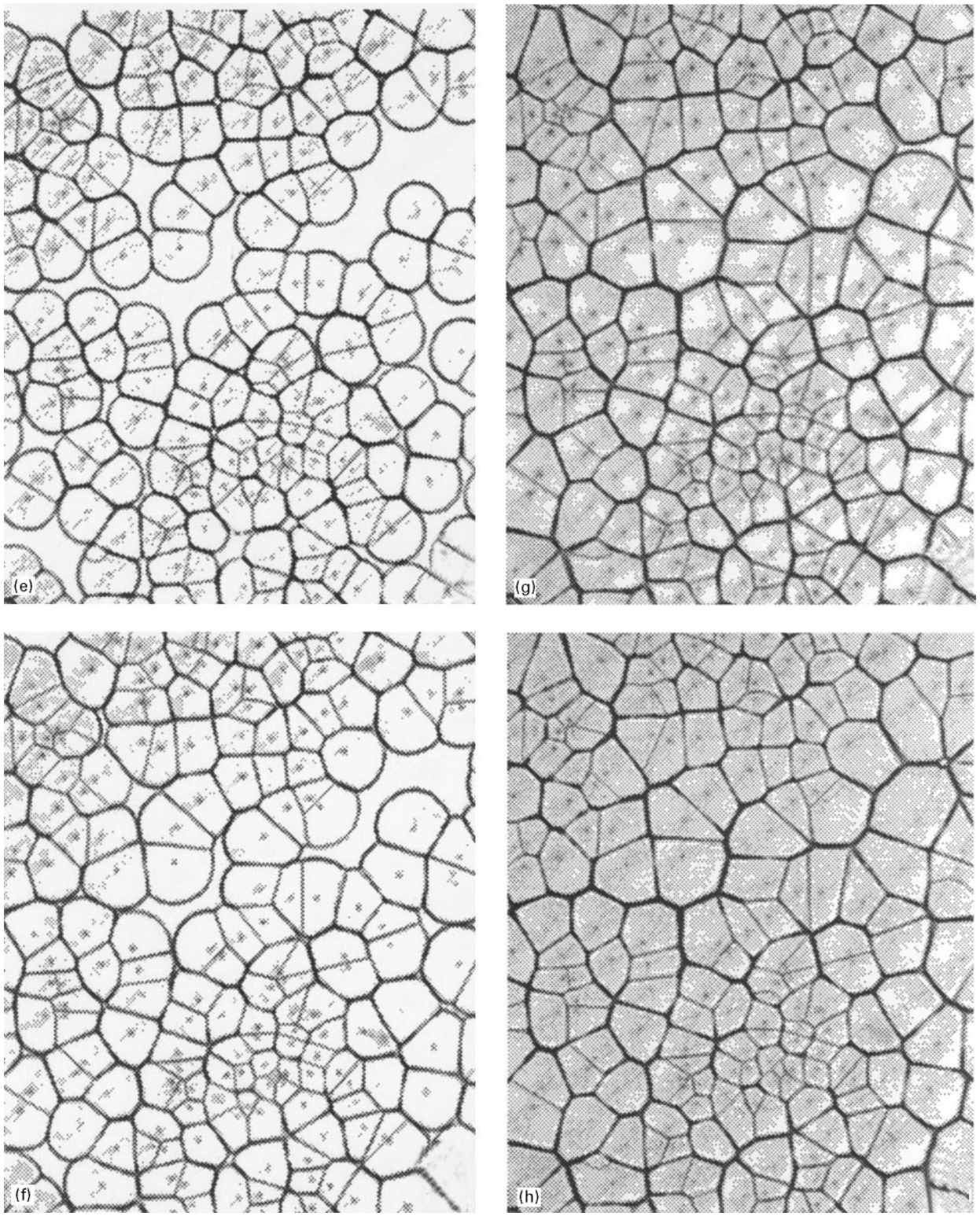

Figure 2 (continued).

$$M_k(n, \mathrm{u}) = \frac{1}{N_n} \sum_{j=1} i_{kj}^{\mathrm{u}} \tag{8a}$$

$$M_k(n, \mathrm{u}+\mathrm{c}) = \frac{1}{N_n} \sum_{j=1} (i_{kj}^{\mathrm{u}} + i_{kj}^{\mathrm{c}}) \tag{8b}$$

In order to identify the basic differences between the correlation functions for the grain patterns and the connective-three cellular pattern, one could test the validity of Equation 5 for all the above relationships. First of all, the relation $m(n) = \sum m_l^j(n)/N_n$ always holds by definition.

Secondly, to test the relation $\sum_k M_k(n) = n$, we define the probability of k-sided neighbours of an n-sided grain as $P_k(n)$ and the average numbers of k-sided neighbours as $\langle j_{kj} \rangle$ for n-sided grains. The following relationships hold because of statistical considerations:

$$\sum_k P_k(n) = 1 \text{ and } \langle i_{kj}^{\mathrm{u}} \rangle = \frac{1}{N_n} \sum_{j=1}^{N_n} i_{kj}^{\mathrm{u}} = P_k(n) \times n \tag{9}$$

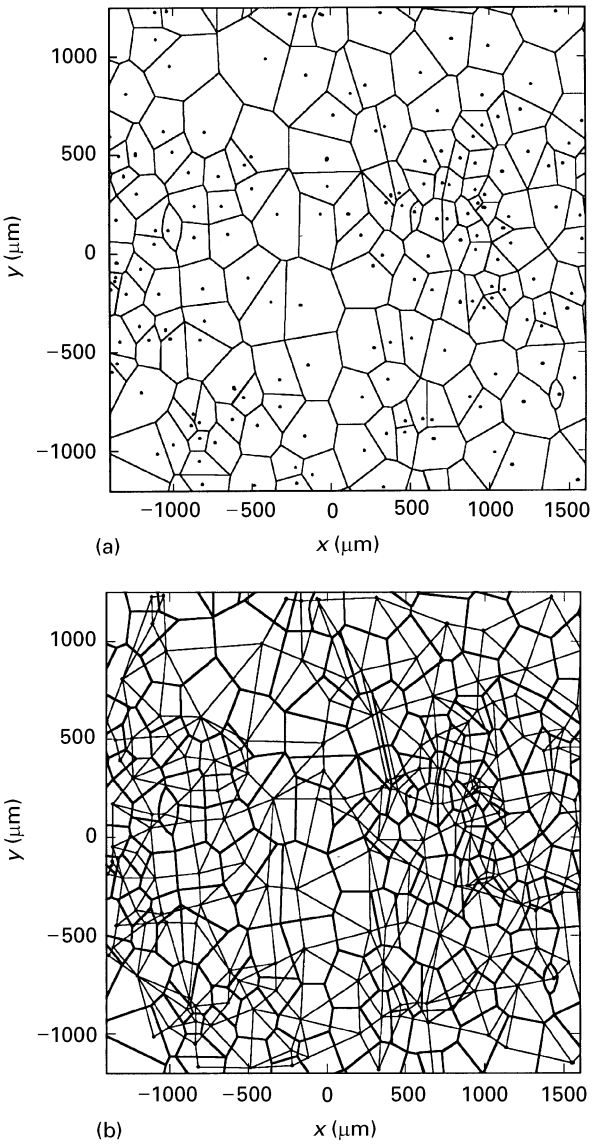

Figure 3 The relationships between the GBN and the corresponding NNN of nuclei centre points: (a) the 2D GBN obtained by edge tracking the image of Fig. 2h; (b) the combination of the GBN and the NNN constructed by nearest-neighbour searching.

Hence, for unconditional neighbours, we find that

$$\begin{aligned}\sum_k M_k(n) &= \sum_k \left(\frac{1}{N_n}\sum_{j=1}^{N_n} i_{kj}^{\mathrm{u}}\right) = \sum_k \langle i_{kj}^{\mathrm{u}}\rangle \\ &= \sum_k \{P_k(n)\times n\} \\ &= n\times\left(\sum_k P_k(n)\right) \\ &= n \qquad (10a)\end{aligned}$$

but, for unconditional plus conditional neighbours, we find that

$$\begin{aligned}\sum_k M_k(n,\mathrm{u}+\mathrm{c}) &= \sum_k \left(\frac{1}{N_n}\sum_{j=1}^{N_n}(i_{kj}^{\mathrm{u}}+i_{kj}^{\mathrm{c}})\right) \\ &= \sum_k M_k(n,\mathrm{u}) + \sum_k \left(\frac{1}{N_n}\sum_{j=1}^{N_n} i_{kj}^{\mathrm{c}}\right) \\ &= n + \sum_k \left(\frac{1}{N_n}\sum_{j=1}^{N_n} i_{kj}^{\mathrm{c}}\right) \\ &> n \qquad (10b)\end{aligned}$$

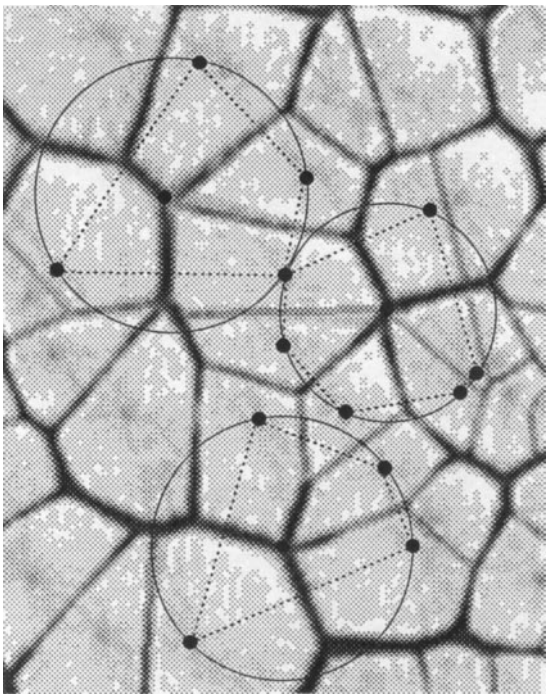

Figure 4 A local image taken from Fig. 2h.

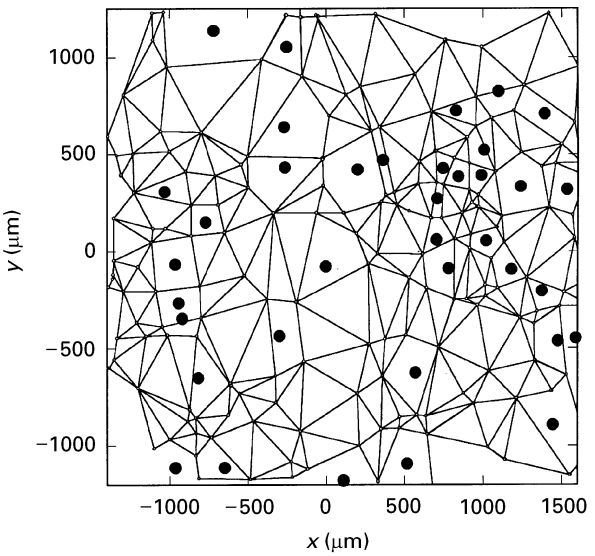

Figure 5 The full circles on the faces of the NNN indicate polygons, which are not triangles.

Thirdly, to test the relation $nm(n) = \sum_k M_k(n)k$, we have the following:

$$\begin{aligned}nm(n,\mathrm{u}) &= \frac{n}{N_n}\sum_{j=1}^{N_n} m_l(n,\mathrm{u}) \\ &= \frac{1}{N_n}\sum_{j=1}^{N_n}\sum_{k=3}(i_{kj}^{\mathrm{u}}\times k) \qquad (11a)\end{aligned}$$

and

$$\begin{aligned}\sum_{k=3} M_k(n,\mathrm{u})\times k &= \frac{1}{N_n}\sum_{k=3}\left(\sum_{j=1}^{N_n} i_{kj}^{\mathrm{u}}\right)\times k \\ &= \frac{1}{N_n}[i_{kj}^{\mathrm{u}}][k] \\ &= \frac{1}{N_n}\sum_{j=1}^{N_n}\sum_{k=3}(i_{kj}^{\mathrm{u}}\times k) \qquad (11b)\end{aligned}$$

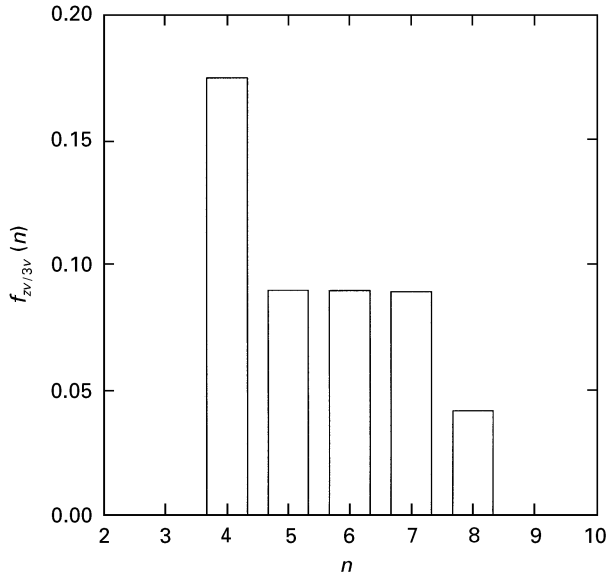

Figure 6 The ratio of $z > 3$ vertices to $z = 3$ vertices corresponding to the number of grain sides, n, in iPP spherulitic grains.

where $[i^{u}_{kj}]$ is a matrix of order $k \times N_n$, and $[k]$ is a one column matrix. Comparing Equations 11a and 11b shows that the relation $nm(n) = \sum_k M_k(n)k$ is valid for unconditional neighbours.

For unconditional plus conditional neighbours, similar computations yield

$$nm(n, \mathrm{u} + \mathrm{c}) = \frac{n}{N_n} \sum_{j=1}^{N_n} m_l(n, \mathrm{u} + \mathrm{c}) = \frac{1}{N_n} \sum_{j=1}^{N_n} \sum_{k=3} \left(\frac{n}{n + l_c} (i^{u}_{kj} + i^{c}_{kj}) \times k \right) \quad (12a)$$

$$\sum_{k=3} M_k(n, \mathrm{u} + \mathrm{c}) \times k = \frac{1}{N_n} \sum_{k=3} \sum_{j=1}^{N_n} (i^{u}_{kj} + i^{c}_{kj}) \times k \quad (12b)$$

so that $nm(n, \mathrm{u} + \mathrm{c}) \neq \sum_k M_k(n, \mathrm{u} + \mathrm{c})k$ for unconditional plus conditional neighbours.

Representative experimental data regarding the correlation between k-sided neighbours of n-sided grains are compared with the above theoretical results in the example shown in Table I, which describes the sequence of the statistical details and analyses applied to the experimental data. The statistical data in Table I relate to the observed characteristics of five-sided grains in one selected image (Fig. 1h). The number of five-sided grains is $N_{n=5} = 40$, among about 200 grains in this image. The neighbouring k-sided grains have $k = 4, 5, 6, 7, 8$. Table I is organized as follows:

(i) The first column is the identification number, n_j, of the five-sided grain.

(ii) The middle columns of Table I provide the statistical data from the experiments, which indicate the numbers of k-sided neighbours of the corresponding five-sided grains.

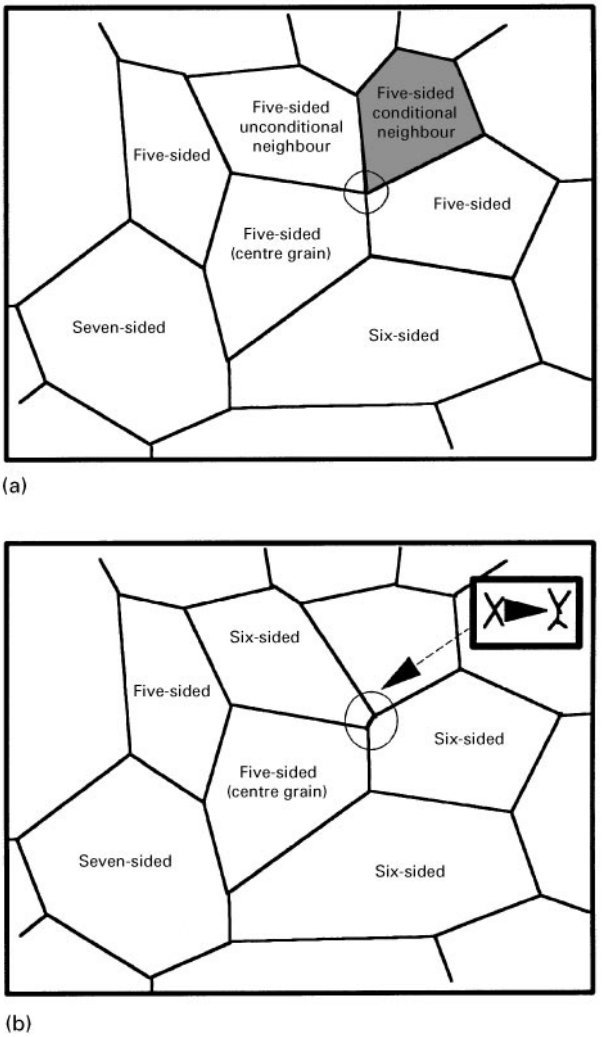

Figure 7 A diagram used to analyse the influences of the singular vertices on the local grain correlation. (a) The central five-sided grain has one conditional neighbour (the dotted grain) which is a five-sided grain that shares one four-fold vertex with the five-sided central grain. (b) After vertex decay, the multiple vertices transform to three-connective vertices.

(iii) The last two columns on the right give the local grain correlation, $m^j_l(5, \mathrm{u})$ and $m^j_l(5, \mathrm{u} + \mathrm{c})$, which are calculated using Equations 6a and 6b for the unconditional and the unconditional plus conditional neighbours, respectively.

(iv) $m_l(5, \mathrm{u})$ and $m_l(5, \mathrm{u} + \mathrm{c})$ are presented in the right bottom corner of Table I.

(v) the bottom row gives the two-grain correlations, $M_k(5, \mathrm{u})$ and $M_k(5, \mathrm{u} + \mathrm{c})$, which are calculated using Equations 8a and 8b for the unconditional and the unconditional plus conditional neighbours, respectively.

For example, the fourth row in Table I shows that the neighbours of the five-sided grain with $(n_j = 1)$ are one four-sided grain $(i_{4u} = 1)$, two five-sided grains $(i_{5u} = 2)$, and two six-sided grains $(i_{6u} = 2)$, so that $m^j_l(5, \mathrm{u}) = (1 \times 4 + 2 \times 5 + 2 \times 6)/5 = 5.2$. In the same way, we get the values of $m^j_l(5, \mathrm{u})$ for $n_j = 1$ to $n_j = 40$, which are listed in the right column of Table I, so that the average $m^j_l(5, \mathrm{u})$ is $m_l(5, \mathrm{u}) = \sum m^j_l(5, \mathrm{u})/40 = 5.7$ (see the bottom right corner of Table I). Furthermore, for all the four-sided neighbour $k = 4$ of the considered five-sided grains, $M_k(5, \mathrm{u}) = \sum i_{4u}/40 =$

TABLE I The correlations between k-sided neighbours of n-sided grains (e.g., $n = 5$)

n grain identification number, n_j	Number of k-sided neighbours of n-sided grain, i_k												m_l (5)	
	$k=3$		$k=4$		$k=5$		$k=6$		$k=7$		$k=8$		$m_l(5, \mathrm{u})$; $(l=n)$	$m_l(5, \mathrm{u}+\mathrm{c})$ $(l=n+l_c)$
	i_u	i_c	i_{ku}	i_{kc}	i_{ku}	i_{kc}	i_{ku}	i_{kc}	i_{ku}	i_{kc}	i_{ku}	i_c		
1			1		2		2						5.2	5.2
2					3		1				1		5.8	5.8
3			1		2		1				1		5.6	5.6
4			1		2		1				1		5.6	5.6
5				1	2	1	3						5.6	5.2
6					2	2	3						5.6	5.429
7			1	1	1		2	1	1				5.6	5.429
8					2		3						5.6	5.6
9			2		1		1	1	1				5.2	5.33
10			1		2		2						5.2	5.2
11					1		2		2				6.2	6.2
12					2		1		2				6.0	6.0
13					3		1		1				5.6	5.6
14							4		1				6.2	6.2
15					1		3		1				6.0	6.0
16					2		1	1	1		1		6.2	6.167
17					1		2	1	1		1		6.4	6.33
18			1		1				1		2		6.4	6.4
19					2		3						5.6	5.6
20					3		1				1		5.8	5.8
21					3	1			1		1		6.0	5.83
22					4		1						5.2	5.2
23				1	3	1	2			1			5.4	5.375
24			1		1	1	2		1				5.6	5.5
25			1			1	3		1				5.8	5.67
26			1	1	1		2		1				5.6	5.33
27			2	1	2				1	1			5.0	5.14
28			2		1	1	1	1	1				5.2	5.29
29			2	1	2	1			1				5.0	4.86
30				2	3		2						5.4	5.0
31			1		2		1				1		5.6	5.6
32			2		2					1	1		5.2	5.5
33					2		1		1		1		6.2	6.2
34			1		2		1		1				5.4	5.4
35			2		1		1	2	1				5.2	5.43
36			1				3	1	1				5.8	5.83
37			2	1		1	2	2	1				5.4	5.375
38					1		2		1		1		6.4	6.4
39					2				2		1		6.4	6.4
40					1		1		1		2		6.8	6.8
$N_n = 40$			$\Sigma i_u = 26$	$\Sigma(i_u + i_c) = 35$	$\Sigma i_u = 68$	$\Sigma(i_u + i_c) = 78$	$\Sigma i_u = 62$	$\Sigma(i_u + i_c) = 72$	$\Sigma i_u = 28$	$\Sigma(i_u + i_c) = 31$	$\Sigma i_u = 16$		$m(5, \mathrm{u}) = 5.7$	$m(5, \mathrm{u}+\mathrm{c}) = 5.6705$
$M_k(5)$			0.65	0.85	1.7	1.95	1.6	1.85	0.7	0.76	0.4			

TABLE II The correlations calculated from Table I

Unconditional neighbours			Unconditional + conditional neighbours		
$\Sigma_k M_k(5, \mathrm{u})$	$m(5, \mathrm{u})$	$\Sigma_k M_k(5, \mathrm{u}) k/n$	$\Sigma_k M_k(5, \mathrm{u}+\mathrm{c})$	$m(5, \mathrm{u}+\mathrm{c})$	$\Sigma_k M_k(5, \mathrm{u}+\mathrm{c}) k/n$
$5 = n$	5.7	$5.7 = m(5, \mathrm{u})$	5.4	5.6705	$5.955 \neq m(5, \mathrm{u}+\mathrm{c})$

$26/40 = 0.65$ (see the bottom row and the fourth column).

Table II shows the results of calculations based on the experimental data of Table I for $M_k(5, \mathrm{u})$ and $m_l(5, \mathrm{u})$. These experimental data and similar analysis performed on a large scale (5000 grains) show that the relations in Equation 5 are valid only for unconditional neighbours; however, they are not valid for unconditional plus conditional neighbours.

5.3. Topological relations

As discussed in Section 3.2, $m(n)$ is the most important topological parameter that can be measured in

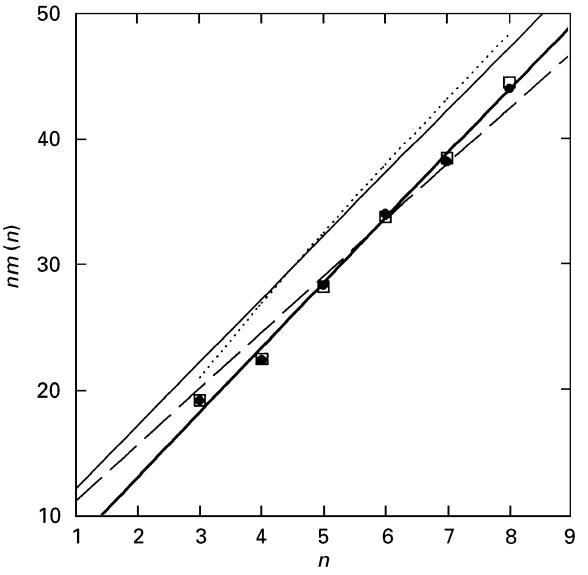

Figure 8 The plot $nm(n)$ versus n of experimental results of iPP spherulitic grain pattern formed at 135 ± 0.1 °C during isothermal crystallization in the simultaneous nucleation case. (●), pure unconditional neighbours; (□), unconditional plus conditional neighbours; (———), regression; (——), the Aboav–Weaire law; (·····), Poisson-Voronoi; (– –), topological model.

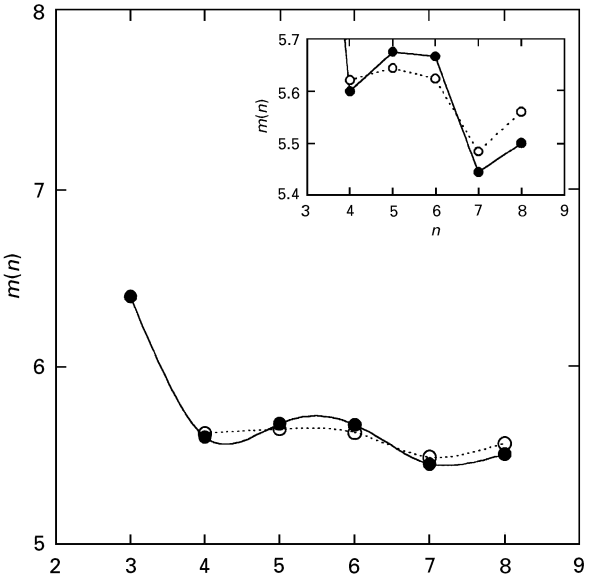

Figure 9 The curves of $m(n)$ versus n for the pure unconditional local grain correlation, $m_l(n, \mathrm{u})$ (●), and the unconditional plus conditional local grain correlation, $m_l(n, \mathrm{u} + \mathrm{c})$ (○), of iPP spherulitic grain pattern formed at 135 ± 0.1 °C during isothermal crystallization in the simultaneous nucleation case, which is shown in Fig. 2.

experiments. In this section, we analyse the experimental data with respect to the Aboav–Weaire relation. Fig. 8 shows $nm(n)$ as a function of n for unconditional neighbours, and unconditional plus conditional neighbours, respectively. We find a linear regression relation $nm(n) = 5.0503n + 3.2376$, for the unconditional neighbour, with the correlation coefficient $R = 0.9974$. The plots of $nm(n)$ versus n for unconditional neighbours and for unconditional neighbours plus unconditional neighbours are almost identical. Comparing this experimental fit with Equation 1, it is found that the slope is nearly 5. The constant a is normally chosen to be 1 for the Aboav–Weaire law [3], but we find that $a = 6 - 5.0503 = 0.9497$. We also find that the intercept is not $6a + \mu_2$, where the second moment, $\mu_2 = 1.233$, is calculated using $\mu_2 = \sum_n P(n)(n - \langle n \rangle)^2$, where $\langle n \rangle$ is the average with respect to the same grain side distribution, $P(n)$. This means that there is a deviation between the experimental results of the iPP spherulitic grain pattern and the Aboav–Weaire law.

We compare the experimental data with Equation 2, which is the theoretical result of 2D simulation of the Poisson–Voronoi diagram, as shown by the dotted line in Fig. 8. The disagreement between the experimental data and this line shows that the iPP spherulitic grain pattern is not a Voronoi diagram. Because the experimental value for the number of the sides of the iPP spherulitic grain pattern is not 6 ($\langle n \rangle = 5.445$), we also compare the experimental data with Equation 3, which is the relation $nm(n)$ versus n for finite networks ($\langle n \rangle \neq 6$) from the topological model [15], as shown by the broken line in Fig. 8. The comparison shows that the experimental data fall close to the broken line representing the theoretical prediction of the topological model. However, the slope of the broken line is that $\langle n \rangle - a = 5.445 - 0.9497 = 4.4953$, which is significantly different from 5, as indicated by experimental data.

In order to explore the above discrepancies between the experimental data and the Aboav–Weaire relation, we have to consider the contribution of the topological defects (the singular vertices) to the Aboav–Weaire relation by exploring the local grain correlation and the two-brain correlation functions. Fig. 9 presents the curves of $m(n)$ versus n for the pure unconditional local grain correlation, $m_l(n, \mathrm{u})$, and for the unconditional plus conditional local grain correlation, $m_l(n, \mathrm{u} + \mathrm{c})$, of iPP spherulitic grain pattern formed at 135 ± 0.1 °C during isothermal crystallization in the simultaneous nucleation case, shown in Fig. 2. The pure unconditional local grain correlation, $m_l(n, \mathrm{u})$, and the unconditional plus conditional local-grain correlation, $m_l(n, \mathrm{u} + \mathrm{c})$, are almost identical. Fig. 9 shows that the curves of $m(n)$ versus n are not smooth, as in the case of cellular structures with all the trivalent vertices. This non-linearity can be concealed by plotting $nm(n)$ versus n as shown in Fig. 8.

Because the common practice of plotting $nm(n)$ versus n can conceal deviations from the Aboav–Weaire law as $m(n)$ does not vary much with n, we shall focus on the two-grain correlation, $M_k(n)$, to explore the details. Fig. 10 shows that two-grain correlations, $M_k(n)$, are clearly non-linear with n for the iPP spherulitic grain pattern. It shows that $M_k(n, \mathrm{u} + \mathrm{c})$ is larger than $M_k(n, \mathrm{u})$. It has been argued that the Aboav–Weaire law is a consequence of a linear correlation function, $M_k(n) = A_k + B_k n$, which obviously yields a linear relation between $nm(n)$ and n for all k, and that maximizes the entropy by reducing the number of constraints [10]. Such correlations are based on purely topological arguments [10–17], where the area and perimeter of the cells are not

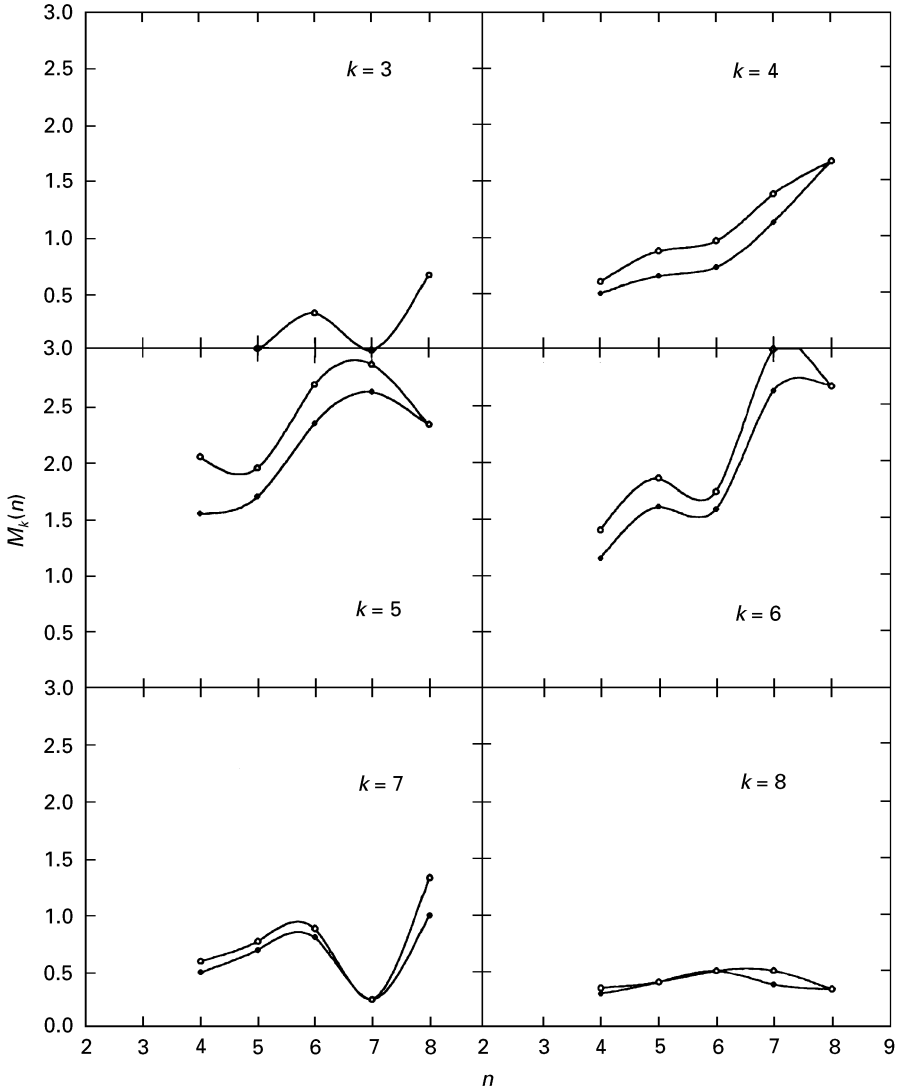

Figure 10 The two-grain correlations, $M_k(n, \mathrm{u} + \mathrm{c})$ (○) and $M_k(n, \mathrm{u})$ (●), of iPP spherulitic grain pattern formed at $135 \pm 0.1\,^{\circ}\mathrm{C}$ during isothermal crystallization in the simultaneous nucleation case.

considered. The results that we presented above show that the Aboav–Weaire relation is seemingly linear, but it does not present linear two-cell correlations. The main difference between most of the real cellular systems and topological models lies in the explicit consideration of area, perimeter and number of sides. These three variables cannot be trivially decoupled. Purely topological models do not incorporate this competition between topology, geometry and growth dynamics and does not seem to be suitable to describe the polymer spherulitic grain pattern.

6. Geometrical and topological correlation

In order to obtain a better understanding and microstructural quantification of polymer spherulitic grain patterns, we study the geometrical properties and the dynamic processes of topological rearrangement.

Fig. 11 plots the experimental data for the average grain area, $\langle a_n \rangle$, as a function of n for the grain pattern shown in Fig. 2. It clearly shows that the Lewis law is not satisfied because the polymer spherulitic grain is an assembly of grains with different sizes. The Lewis plot is S-shaped owing to the polydisperse grain packing. This means that the correlation between the sides and the areas is non-linear. An extensive study of this correlation between the grain sizes and the shapes is currently under investigation.

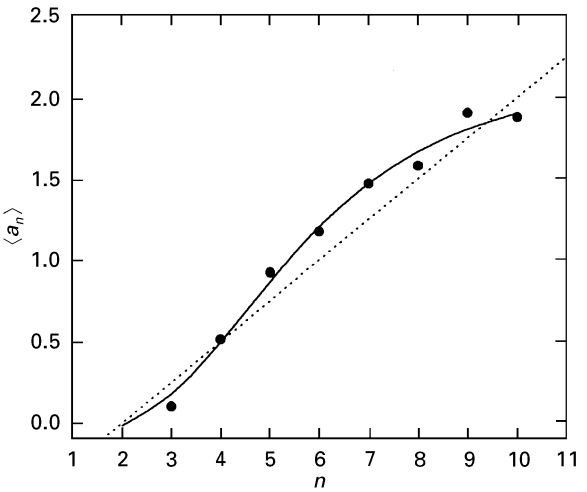

Figure 11 The experimental results (●) of the average grain area, $\langle a_n \rangle$, as a function of n for iPP spherulitic grain pattern formed at $135 \pm 0.1\,^{\circ}\mathrm{C}$ during isothermal crystallization in the simultaneous nucleation case. (- - - - -), the Lewis law.

As mentioned in Section 2.2, the network of polymer polygrains does not exhibit any detectable changes in a practical time scale at room temperature. *In situ* observation of topological rearrangements of the GBNs of polymer spherulitic grains shows that there are some topological changes during thermal activation experiments at higher temperatures (higher than the crystallization temperature but below the melting point) over long times. There are two useful characteristics of a 2D grain: grain area, A, and its topological class, n (the number of sides in the grain). The ensemble of grains may be described in the phase space (n, A) by introducing a one-particle density function, $F_n(A, t)$, giving the mean number of grains of the topological class, n, and area, A, per unit area of a 2D grain pattern at the moment of time, t. Fradkov *et al.* [11] introduced a new function

$$\left\langle n\left(\frac{A}{\langle A\rangle}\right)\right\rangle = \sum_n nF_n(A, t)/\sum_n F_n(A, t) \quad (13)$$

The function $\langle n(A/\langle A\rangle)\rangle$ expresses the area-topological class correlation, where $A/\langle A\rangle$ is normalized grain area and $\langle A\rangle$ is the average value of grain area. Extrapolation of the experimental dependence $\langle n(A/\langle A\rangle)\rangle$ to $A/\langle A\rangle = 0$ gives the mean value of the topological class of the vanishing grains. Fig. 12 shows the experimental results of the dependence of mean topological class of grains $\langle n(A/\langle A\rangle)\rangle$ on normalized grain area. Fig. 13 shows that the intercept is close to $\langle n(A/\langle A\rangle)\rangle = 4.003\,87$; thus, the most unstable grains are four-sided grains.

We have observed that the most likely change in polymer grain shapes is the decay of multiple vertices by the addition of edges at the vertex to form short sides during the thermal activation experiment. Fig. 13 shows that a four-sided grain changes its shape and another loses one edge to a neighbour that changes its shape during the thermal activation experiment at $T = 150\,^{\circ}\mathrm{C}$ of the sample of iPP spherulitic grain pattern formed at $135 \pm 0.1\,^{\circ}\mathrm{C}$. A non-convex

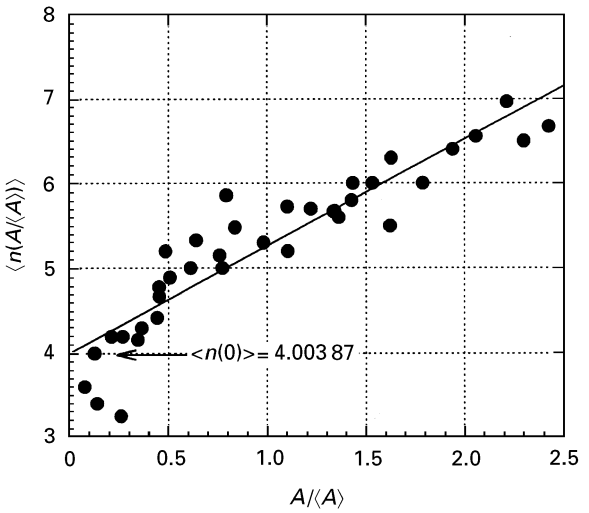

Figure 12 The experimental results of the dependence of mean topological class of grains, $\langle n\rangle$, on the normalized grain area of iPP spherulitic grain pattern formed at $135 \pm 0.1\,^{\circ}\mathrm{C}$ during isothermal crystallization in the simultaneous nucleation case.

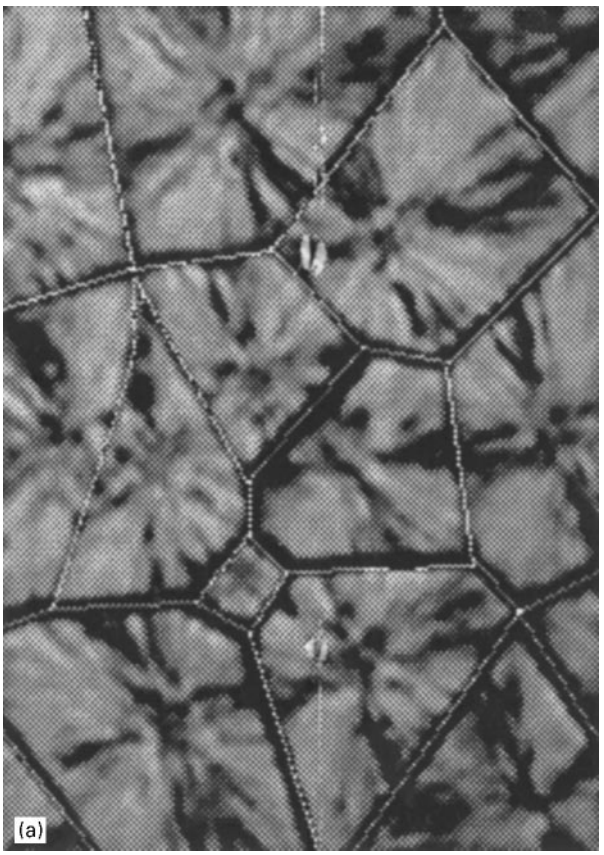

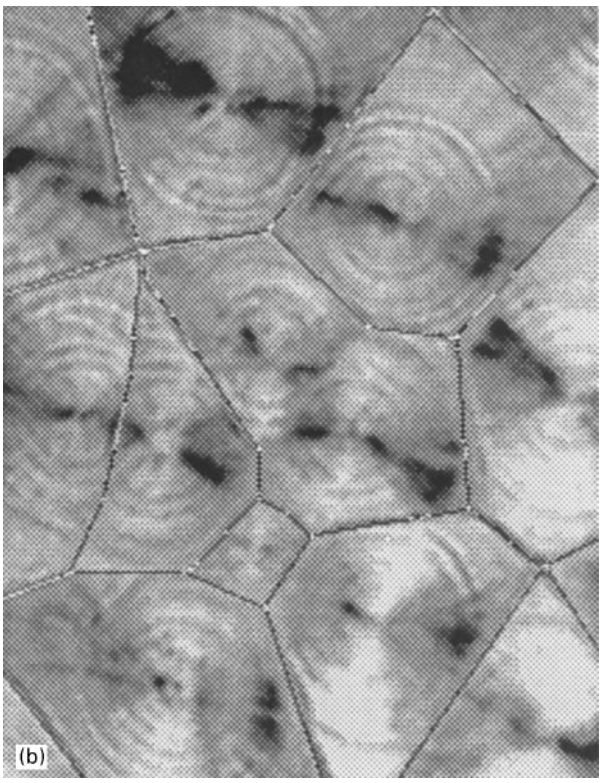

Figure 13 A four-sided grain losing one edge to a neighbour that changes its shape during the thermal activation experiment at $T = 150\,^{\circ}\mathrm{C}$ of the sample of iPP spherulitic grain pattern formed at $135 \pm 0.1\,^{\circ}\mathrm{C}$: (a) before activation experiment; (b) after activation experiment.

polygon-shaped grain seen in Fig. 13, which is the amalgamation of one four-sided grain and one of its neighbours, was observed after the process of losing one edge was finished. Therefore, Fig. 13 appears to confirm the prediction of Fig. 12. Unlike soap froth

and 2D normal grain growth of polygrain in metals, no grain disappearance or grain shrinkage [8] and no topological cascade of neighbour switching [8] are observed is polymer spherulitic grain systems.

7. General remarks

The above experiments and analysis suggest that the distinguishing features of topological properties of polymer grains are due to the topological defects and the lack of mobility of the polymer grain boundary system. Topological defects do not exist or are only short lived in other systems, but in polymer grains they are fairly permanent. The polymer grain-boundary mobility is dependent on the submacromolecular organization of grain boundaries and inside texture of the spherulite. The spherulites consist of individual lamellar crystalline plates with amorphous material in the space between the lamellar structures. However, little is known about the submacromolecular organization of the spherulitic grain-boundary region. The highly complex grain boundaries are inhomogeneous, owing to the possible discontinuities between crystalline–crystalline and crystalline–amorphous phases and the continuity of the amorphous phase. The relative orientations of neighbouring grains, the orientation of the boundary surface itself with respect to the two grains, and the unknown surface tension of the grain boundary are all involved in the grain-boundary motion. The movement of the spherulitic grain boundaries may be coupled with the secondary crystallization in the grain-boundary region. The loss or disappearance of a side could be due to the matching of the crystalline–crystalline and amorphous–amorphous phases of the neighbouring grains. Owing to the slow dynamics of macromolecular diffusion across and along the grain boundary, the uniform grain-boundary mobility is quite slow. When the anisotropy at some location is too large, the vertex boundary conditions are no longer strong enough to produce curvature in grain boundaries, and the mobility may be zero. A possible mechanism for the grain-boundary motion is due to the impingement process which has a relatively high energy. The grain boundary relaxes to a lower-energy structure with a reduction in unfavourable polymer chain conformations. Other driving forces for grain-boundary motion, especially at relatively high temperatures, may include unrelaxed stress fields and the curvature elasticity of the lamellae contained within spherulite.

The differences between polymer spherulitic grain patterns and small molecule cellular systems are essentially due to the differences in their molecular dynamic characteristics. Because they are the long flexible macromolecules, the corresponding collective length scale for polymer polygrain structures is distinctly larger. Therefore, the dynamic phenomena are very much slower.

8. Conclusions

An experimental investigation of large-scale (around 5000 grains per samples) pattern formation of polymer spherulitic grains was carried out under simultaneous nucleation conditions. Comprehensive image analysis was performed on the topological correlation and geometrical distributions of grain boundary shapes and grain sizes, as well as on the topological rearrangement during thermal activation experiments. The new findings are as follows.

1. The multiple-graphic construction of GBNs and the NNNs indicate that the topological properties are significantly different from other 2D cellular structures because of the observation of a higher percentage of multiple vertices. It is shown that polymeric GBNs are different from the classical Voronoi diagram because the NNNs are an incomplete connectivity-three graph.

2. Multiple vertices are singular topological defects that introduce new features in topological correlation functions. Statistical analysis and experimental data show that the fundamental relationships of topological correlation parameters, which are expressed in Equation 5, are valid for unconditional neighbours, but invalid for unconditional plus conditional neighbours.

3. The experimental data of spherulitic polygrain structures seemingly yield a linear Aboav–Weaire relation, which states that, on average, the sum of the number of sides of the cells immediately adjacent to an n-sided grain, $nm(n)$ is linear in n, with a slope very near 5. However, the intercept is not "$6a + \mu_2$", where μ_2 is the second moment, and where the constant a is around 1.

4. The two-cell correlation functions, $M_k(n)$ (the average number of k-sided grains adjoining an n-sided grain), are clearly highly, non-linear with n. It is important to analyse the non-linearity of $M_k(n)$ to evaluate the topological correlation because $nm(n) = \sum_k M_k(n)k$. The common practice of plotting $nm(n)$ versus n can conceal deviations of the non-linearity of the experimental data.

5. It is very valuable to study the geometrical properties and the dynamic processes of topological rearrangements for understanding the dynamic correlation between the geometry and topology of polymer spherulitic grain patterns. Experimental results show that the Lewis plot (the relation of average area of grains to the number of sides) is non-linear and S-shaped owing to the polydisperse grain packing. Experimental observations and statistical data show that extrapolation of the dependence of the mean topological class of grains, $\langle n \rangle$, on normalized grain area indicates the mean topological class for vanishing grains to be about $\langle n \rangle = 4$. This means that the four-sided grains are the most unstable grains.

6. The distinguishing features of topological properties of polymer grains are due to the topological defects and the lack of mobility of the polymer grain-boundary system. The results of this work indicate that polymer grain systems are topologically unstable structures that evolve slowly. It is difficult for polymer spherulitic grains to relax from multiple vertices to the trivalent vertices and, ultimately, to a stationary cellular structure.

Acknowledgements

This work was supported by research grants from the Natural Science and Engineering Research Council of Canada and the Ministere de l'Education, Gouvernement du Quebec. T.H. appreciates the partial support from the Aerospace Administration of the People's Republic of China.

References

1. T. HUANG, M. R. KAMAL and A. D. REY, *J. Mater. Sci. Lett*. **14** (1995) 220.
2. T. HUANG, A. D. REY and M. R. KAMAL, in "Grain-size and mechanical properties – fundamentals and applications", edited by M. A. Otooni, R. W. Armstrong, N. J. Grant and K. Ishizari, Materials Research Society Symposium Proceedings (Materials Research Society, Pittsburgh, PA, 1995) Vol. 362, p. 193.
3. D. WEAIRE and N. RIVIER, *Contemp. Phys.* **25** (1984) 59.
4. J. STAVANS, *Rep. Prog. Phys.* **56** (1993) 733.
5. J. STAVANS and J. A. GLAZIER, *Phys. Rev. Lett*. **62** (1989) 1318.
6. J. A. GLAZIER, M. P. ANDERSON and G. S. GREST, *Phil. Mag., B* **62** (1990) 615.
7. V. E. FRADKOV, M. E. GLICKSMAN, M. PALMER, J. NORDBERGAND and K. RAJAN, *Physica D* **66** (1993) 50.
8. *Idem., Acta Metall. Mater*. **42** (1994) 2719.
9. V. E. FRADKOV and D. G. UDLER, *Adv. Phys.* **43** (1994) 739.
10. N. RIVIER, *Phil. Mag. B* **52** (1985) 795.
11. V. E. FRADKOV, L. S. SHVINDLERMAN and D. G. UDLER, *Phil. Mag. Lett*. **55** (1987) 298.
12. M. A. PESHKIN, K. J. STRANDBURG and N. RIVIER, *Phys. Rev. Lett*. **67** (1991) 1803.
13. C. GODRECHE, I. KOSTOV and I. YEKUTIELI, *ibid.* **67** (1992) 2674.
14. R. DELANNAY, G. LE CAER and M. KHATUN, *J. Phys. A: Math. Gen.* **25** (1992) 6193.
15. G. LE CAER and R. DELANNAY, *ibid.* **26** (1993) 3931.
16. R. DELANNAY and G. LE CAER, *Phys. Rev. Lett*. **73** (1994) 1553.
17. M. O. MAGNASCO, *Phil. Mag. B* **65** (1992) 895.
18. F. P. PREPARATA and M. I. SHAMOS, "Computational geometry" (Springer, New York, 1985).
19. S. KUMAR, S. K. KURTZ and D. WEARIE, *Phil. Mag. Lett*. **55** (1987) 289.
20. F. T. LEWIS, *Anat. Rec.* **38** (1928) 341.
21. *Idem., ibid.* **50** (1931) 235.
22. R. M. C. DE ALMEIDA and J. R. IGLESIAS, *Phys. Rev. A* **43** (1991) 2763.
23. J. C. M. MOMBACH, R. M. C. DE ALMEIDA and J. R. IGLESIAS, *Phys. Rev. E* **47** (1993) 3712.
24. H. FLYVBJERG, *ibid.* **47** (1993) 4037.

Received 17 May 1996
Accepted 20 January 1997